

# JGR Space Physics

## RESEARCH ARTICLE

10.1029/2025JA033931

### Key Points:

- Using the Arase satellite data, we conduct both linear and nonlinear theoretical analyses of a chorus event during a substorm injection
- Prior to the substorm injection, chorus waves present weak rising tones; after injection, chorus waves present intense rising-tone elements
- Substorm-injected hot electrons increase the linear growth and reduce the threshold amplitude, driving chorus waves' nonlinear evolution

### Correspondence to:

R. Chen and Y. Miyoshi,  
[rz0112@auburn.edu](mailto:rz0112@auburn.edu);  
[miyoshi@isee.nagoya-u.ac.jp](mailto:miyoshi@isee.nagoya-u.ac.jp)





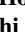

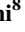





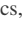
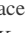
### Citation:

Chen, R., Miyoshi, Y., Zhao, H., Chen, H., Wang, X., Kasahara, Y., et al. (2025). Observational evidence for the nonlinear growth of chorus waves caused by substorm injected energetic electrons. *Journal of Geophysical Research: Space Physics*, 130, e2025JA033931. <https://doi.org/10.1029/2025JA033931>

Received 7 MAR 2025

Accepted 18 JUN 2025

## Observational Evidence for the Nonlinear Growth of Chorus Waves Caused by Substorm Injected Energetic Electrons

Rui Chen<sup>1</sup> , Yoshizumi Miyoshi<sup>2,3</sup> , Hong Zhao<sup>1</sup> , Huayue Chen<sup>1</sup> , Xueyi Wang<sup>1</sup> , Yoshiya Kasahara<sup>4</sup> , Shoya Matsuda<sup>4</sup> , Tomoaki Hori<sup>2</sup> , Fuminori Tsuchiya<sup>5</sup> , Atsushi Kumamoto<sup>5</sup> , Atsuki Shinbori<sup>2</sup> , Satoshi Kasahara<sup>6</sup> , Shoichiro Yokota<sup>7</sup> , Kunihiro Keika<sup>6</sup> , Takefumi Mitani<sup>8</sup> , Takeshi Takashima<sup>8</sup> , Ayako Matsuoka<sup>9</sup> , Mariko Teramoto<sup>10</sup> , Kazuhiro Yamamoto<sup>2</sup> , and Iku Shinohara<sup>8</sup> 

<sup>1</sup>Department of Physics, Auburn University, Auburn, AL, USA, <sup>2</sup>Institute for Space-Earth Environmental Research, Nagoya University, Nagoya, Japan, <sup>3</sup>Kyung Hee University, Swon, South Korea, <sup>4</sup>Kanazawa University, Kanazawa, Japan, <sup>5</sup>Graduate School of Science, Tohoku University, Sendai, Japan, <sup>6</sup>University of Tokyo, Tokyo, Japan, <sup>7</sup>Osaka University, Toyonaka, Japan, <sup>8</sup>Institute of Space and Astronautical Science, Japan Aerospace Exploration Agency, Sagami-hara, Japan, <sup>9</sup>Data Analysis Center for Geomagnetism and Space Magnetism, Graduate School of Science, Kyoto University, Kyoto, Japan, <sup>10</sup>Kyushu Institute of Technology, Iizuka, Japan

**Abstract** Substorm energetic electron injections serve as a significant energy source for chorus wave generation, markedly altering the distribution of energetic electrons. Using the Arase satellite data, we present direct evidence for the nonlinear evolution of chorus waves following a substorm injection. The substorm injection causes the enhancement of energetic electron fluxes ( $\sim 20$ – $200$  keV) during which chorus waves appear as clear and intense rising-tone elements. Linear theoretical analysis shows that anisotropic energetic electrons provide free energy for the generation of seed chorus waves and the enhancement of energetic electrons increases the linear growth rate. Furthermore, nonlinear theoretical analysis shows that the increase in energetic electrons reduces the threshold amplitude, which is conducive to the chorus wave entering the nonlinear growth stage. These results indicate that nonlinear growth plays a significant role in the amplification and spectral evolution of chorus waves through a decrease in the threshold amplitudes.

## 1. Introduction

Whistler mode chorus waves are right-hand polarized electromagnetic waves with frequencies ranging from  $\sim 0.1 f_{ce}$  to  $\sim 0.8 f_{ce}$ , frequently observed outside the plasmasphere where the plasma density is relatively low (e.g., Burtis & Helliwell, 1969; Gao et al., 2014; W. Li et al., 2011; Tsurutani & Smith, 1974). Extensive research over several decades has demonstrated that chorus waves play an important role in regulating electron dynamics within the radiation belts: on one hand, chorus waves are believed to effectively scatter low-energy electrons ( $\sim$ keV to 10s of keV) into the loss cone, causing precipitation into the upper atmosphere and ultimately contributing to the formation of diffuse and pulsating auroras (e.g., R. Chen et al., 2024; Gao et al., 2023; S. Kasahara et al., 2018a; W. Li et al., 2012; Miyoshi et al., 2010, 2020, 2021; Ni et al., 2008; Thorne et al., 2010; Tsurutani et al., 2013); on the other hand, chorus waves interact with energetic electrons through cyclotron resonance, facilitating energy transfer that can accelerate electrons to high energies (from 100s of keV to  $>$  MeV), and thus chorus wave-driven local acceleration is one of the main sources of relativistic electrons in the radiation belts (e.g., Allison & Shprits, 2020; Bortnik & Thorne, 2007; Horne et al., 2005; W. Li et al., 2014; Miyoshi et al., 2003, 2013; Reeves et al., 2013; Thorne et al., 2013; Xiao et al., 2009; Zhao et al., 2018, 2019). The frequency-time spectrum of chorus waves typically appears as a series of discrete, repetitive elements with frequency chirping, for example, rising-tone (upward chirping) or falling-tone (downward chirping) elements (e.g., Gao et al., 2014; W. Li et al., 2011; Tsurutani & Smith, 1974). The repetitive feature of chorus waves is possibly caused by the continuous injection of energetic electrons from the plasma sheet (H. Chen et al., 2022; Gao et al., 2022; Lu et al., 2021).

Chorus waves are generally excited by anisotropic electrons with energies ranging from a few keV to tens of keV, in which both linear and nonlinear processes play an indispensable role in the generation of chorus waves (e.g., H. Chen et al., 2022; Kennel & Petschek, 1966; L. Li et al., 2022; W. Li, Thorne, Angelopoulos, Bonnell, et al., 2009; Omura, 2021; Tsurutani & Smith, 1974; Zhou et al., 2023). It is generally believed that whistler mode waves are initially generated near the magnetic equator at a frequency corresponding to the maximum linear growth rate via

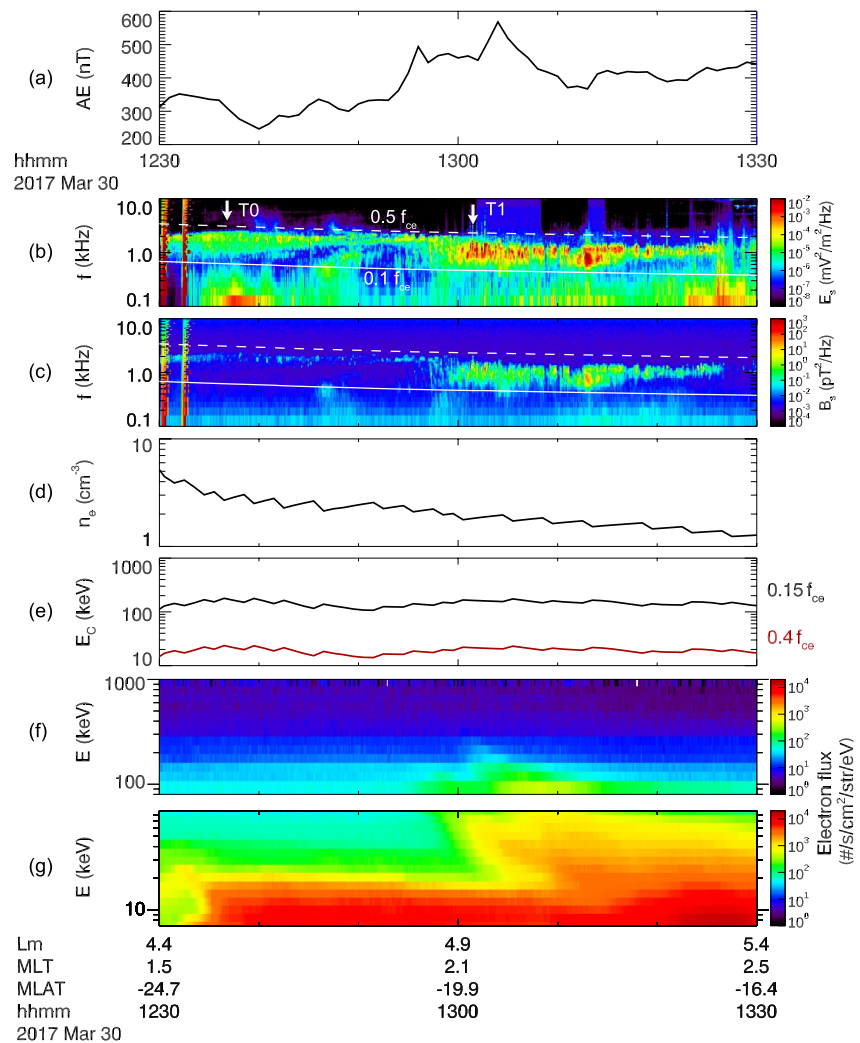
the temperature anisotropy (e.g., Kennel & Petschek, 1966; W. Li, Thorne, Angelopoulos, Bonnell, et al., 2009; Tsurutani & Smith, 1974). The linear growth rate is generally related to two critical factors, that is, anisotropy of energetic electrons in the velocity space and the resonance conditions. The rate of wave growth or damping depends on the fraction of electrons that resonate with the waves and the electron anisotropy: the energetic electron fluxes need to be high, and their anisotropy needs to be large enough to satisfy the cyclotron instability threshold for whistler mode waves (R. Chen et al., 2023; Kennel & Petschek, 1966; W. Li, Thorne, Angelopoulos, Bonnell, et al., 2009). The increase in the anisotropy of energetic electrons enhances the linear growth rate, which has been supported by theoretical and observational studies (e.g., Kennel & Petschek, 1966; W. Li, Thorne, Angelopoulos, Bonnell, et al., 2009). Furthermore, both a lower background magnetic field and a relatively larger plasma density could lead to a lower resonance energy of electrons with whistler mode waves, and thus more energetic electrons could provide more free energy for the generation of whistler mode waves (e.g., R. Chen et al., 2023; W. Li, Thorne, Angelopoulos, Bonnell, et al., 2009).

Observations and simulations have revealed that the generation of chorus waves is often more complex than predicted by linear theoretical models. For instance, chorus waves frequently exhibit fine structures, including frequency chirping for rising-tone or falling-tone elements, which cannot be fully explained by linear theory alone (e.g., Gao et al., 2014; W. Li et al., 2011). These features suggest the importance of nonlinear effects, modifying the growth and saturation of chorus waves (e.g., H. Chen et al., 2022; L. Li et al., 2022; Omura, 2021). According to the theory (e.g., Omura, 2021), the nonlinear growth process is triggered when the wave amplitude of chorus waves exceeds the threshold amplitude. During the process, the nonlinear trapping of resonant electrons results in the formation of an electron hole in the phase space, and the electron hole can form a resonant current that further causes a wave with a rising frequency (e.g., Omura, 2021). Recent numerical simulations have verified the nonlinear growth process of chorus waves and reproduced these waves with rising-tone elements (e.g., H. Chen et al., 2022; Katoh & Omura, 2007; Ke et al., 2017; Lu et al., 2019, 2021; Omura, 2021). In addition, a rising-tone or falling-tone element of chorus waves is composed of several subpackets/subelements (with a duration of about 10 s–100 ms; R. Chen et al., 2022; Santolík et al., 2014; Tsurutani et al., 2020), and the formation of these subpackets/subelements can also be caused by the nonlinear electron trapping through cyclotron resonance (H. Chen et al., 2023, 2024; Nogi & Omura, 2023). As a result, the nonlinear growth process significantly contributes to the generation of chorus waves.

Previous studies have shown that substorm energetic electron injections are one of the energy sources for the generation of chorus waves in the inner magnetosphere (e.g., W. Li, Thorne, Angelopoulos, Bonnell, et al., 2009; W. Li et al., 2010; Ma et al., 2022; Miyoshi et al., 2003, 2007, 2013; Tsurutani & Smith, 1974, 1977). Substorm injections, usually associated with magnetic field dipolarization, significantly change the number density of energetic particles and the configuration of geomagnetic fields, which further affect the generation of chorus waves (e.g., W. Li, Thorne, Angelopoulos, Bonnell, et al., 2009; Miyoshi et al., 2007, 2013). Several global models of chorus waves have been established using satellite observations (such as CRRES, THEMIS, Van Allen Probes, and Arase, e.g., Agapitov et al., 2015; Kazama et al., 2021; W. Li, Thorne, Angelopoulos, Bortnik, et al., 2009; Ma et al., 2022; Meredith et al., 2003; Tsurutani & Smith, 1977; Wang et al., 2019); these observations and models show that the occurrence and intensity of chorus waves strongly depend on substorm activity (represented by AE index). Using THEMIS data, W. Li, Thorne, Angelopoulos, Bonnell, et al. (2009) reported the intensification of chorus waves outside the plasmapause during the injection of anisotropic plasma sheet electrons into the inner magnetosphere, which is consistent with the linear growth process. Moreover, L. Li et al. (2022) presented Van Allen Probes observations of periodic chorus waves in the troughs of compressional ultralow frequency waves during which a substorm injection occurred, leading to the enhancement of the chorus wave intensity and frequency range. To date, few event studies have investigated the impact of substorm injections on chorus wave generation, and the understanding of which parameters are important for linear and nonlinear growth remains limited. In this study, using the Arase satellite data, we present direct evidence for the nonlinear evolution of chorus waves following a substorm injection. We conduct both linear and nonlinear growth analyses to investigate the effects of substorm injection on the generation of chorus waves.

## 2. Data

The Arase satellite operates entirely within the Earth's radiation belts and carries scientific instruments to measure plasma/particle and field/wave data (Miyoshi, Hori et al., 2018; Miyoshi, Shinohara et al., 2018a). In this study, the wave electric and magnetic power spectra with a cadence of one second are provided by Onboard Frequency

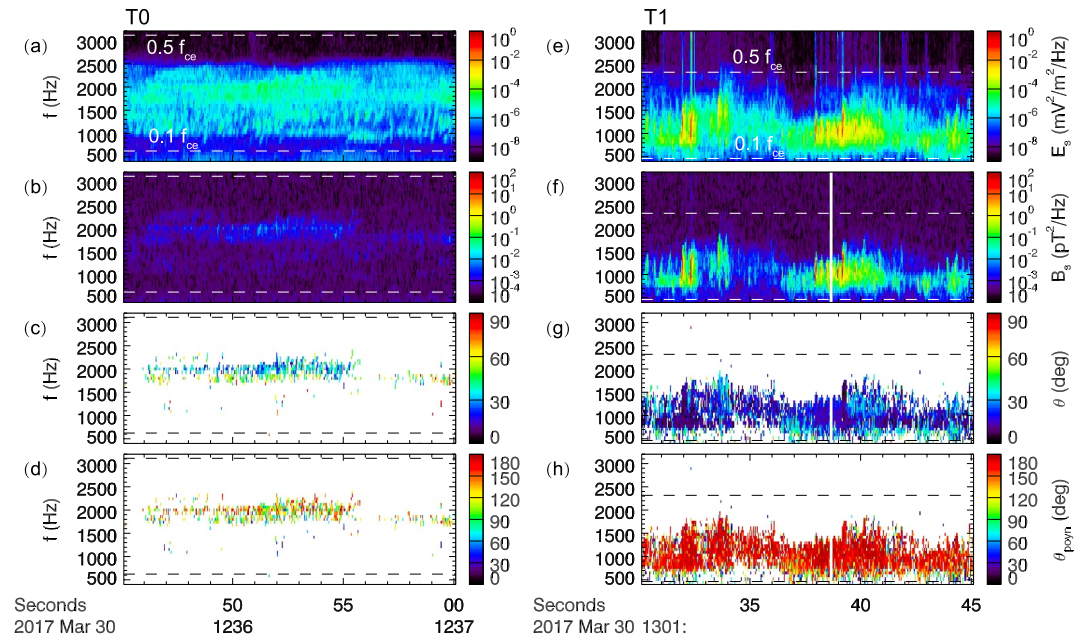


**Figure 1.** (a) AE index, time-frequency spectra of (b) wave electric and (c) magnetic field, (d) background plasma density, (e) minimum resonance energies of electrons interacting with waves at  $0.15$  and  $0.4 f_{ce}$  through first-order cyclotron resonance at the magnetic equator, and (f, g) electron fluxes in the energy range of  $\sim 80$ – $1,000$  keV and  $\sim 7$ – $80$  keV. In panels (b and c), the solid and dashed lines represent  $0.1$  and  $0.5 f_{ce}$ , respectively. Intense emissions in the wide-band frequencies at  $\sim 12:30$  UT are onboard calibration signals (Matsuda et al., 2018).

Analyzer in Plasma Wave Experiment (PWE, Y. Kasahara et al., 2018; Matsuda et al., 2018). The electromagnetic field data measured by Waveform Capture in PWE is used to investigate the waveform of chorus waves (Y. Kasahara et al., 2020a, 2020b). The local magnetic field  $B_{loc}$  measured by the Magnetic Field Experiment (MGF, Matsuoka et al., 2018) is used to estimate the magnetic field  $B_{eq}$  at the magnetic equator ( $B_{eq} = B_{loc} \cdot B_{eq}^{TS05} / B_{loc}^{TS05}$ , where  $B_{eq}^{TS05}$  and  $B_{loc}^{TS05}$  are equatorial and local magnetic fields from the TS05 magnetic field model, Tsyganenko & Sitnov, 2005). The background plasma density can be estimated based on the upper hybrid band measured by the High-Frequency Wave Receiver in PWE (Y. Kasahara et al., 2021; Kumamoto et al., 2018). The velocity-space distribution of electrons in the energy range of  $\sim 10$ – $100$  s of keV are measured by Medium-Energy Particle Experiments-Electron Analyzer (MEPe, S. Kasahara et al., 2018b, 2022) and High-Energy Electron Experiments (HEP, Hori et al., 2020; Mitani et al., 2018). Moreover, the AE index can be obtained in OMNIWeb.

### 3. Observation Results

Figure 1 presents a chorus event during the time interval from 12:30 UT to 13:30 UT on 30 March 2017. At  $\sim 12:43$  UT, a moderate substorm during a CIR-driven storm occurred with the AE index increasing up to

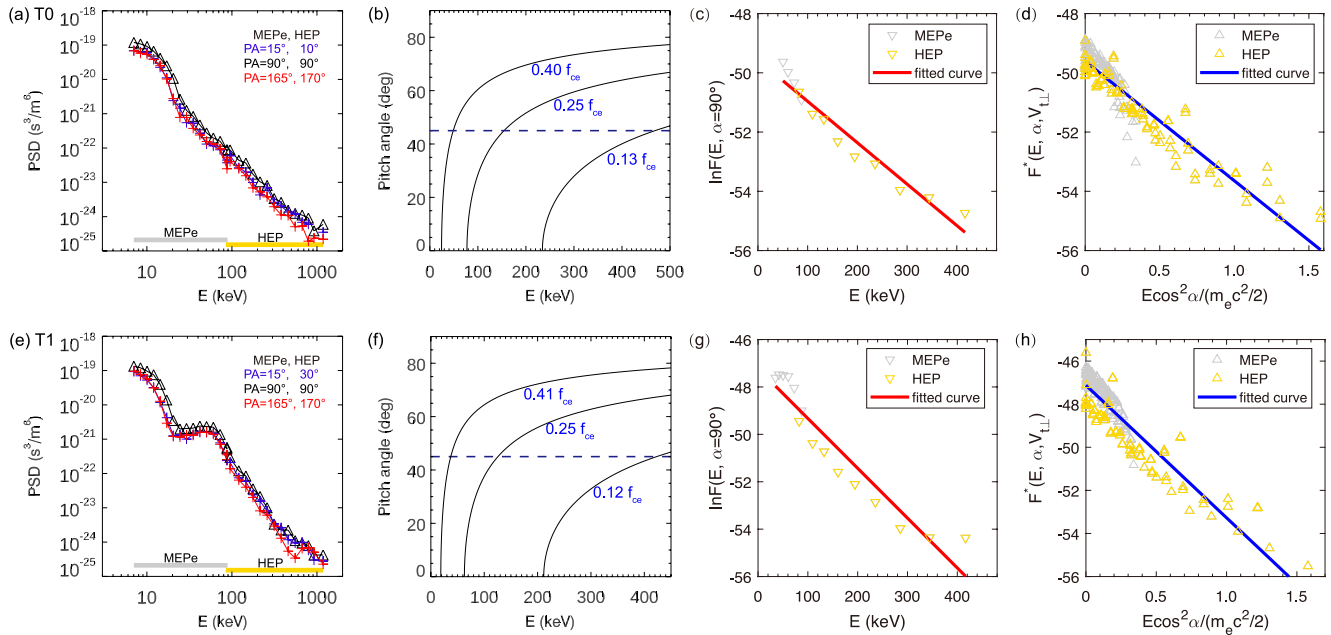


**Figure 2.** Two typical chorus examples observed at T0 and T1 marked in Figure 1b. (a, b) Spectra of wave electric and magnetic fields, (c) wave normal angle  $\theta$  (the angle between wave vector  $\vec{k}$  and background magnetic field  $\vec{B}_0$ ), and (d) Poynting angle  $\theta_{poynt}$  (the angle between the direction of Poynting flux and  $\vec{B}_0$ ). Panels (e–h) show the results for time T1. The locations are at  $L = 4.6$ , MLT = 1.6 hr, MLAT =  $-23.5^\circ$  and  $L = 5.0$ , MLT = 2.1 hr, MLAT =  $-19.6^\circ$  for T0 and T1, respectively.

$\sim 600$  nT (Figure 1a). Chorus waves, in the frequency range between  $\sim 0.1 f_{ce}$  and  $\sim 0.4 f_{ce}$  ( $f_{ce}$  is the equatorial electron gyrofrequency), were observed by the Arase satellite (Figures 1b and 1c). Figure 1d presents the background plasma density (solid line) estimated based on the upper hybrid frequency measured by PWE, which is less than  $10 \text{ cm}^{-3}$  during the time; a sharp drop of plasma density was observed at  $\sim 12:13$  UT (from  $\sim 100$  to  $\sim 10 \text{ cm}^{-3}$ , not shown), indicating the location of the plasmopause. Therefore, these chorus waves are located outside the plasmopause. Based on the cold plasma dispersion relation, the minimum cyclotron resonance energy can be estimated under the first-order cyclotron resonance. Figure 1e shows the minimum cyclotron resonance energies for wave frequencies at  $0.15 f_{ce}$  and  $0.4 f_{ce}$  in the equatorial plane, ranging from tens of keV to  $\sim 100$  keV. Figures 1f and 1g show the electron fluxes in the energy range of  $\sim 7$ – $1,000$  keV. At  $\sim 13:00$  UT, an enhancement of energetic electrons ( $\sim 20$ – $200$  keV) was observed with clear energy dispersion features, that is, the enhancement of high-energy electrons was observed earlier than that of low-energy electrons (Figures 1f and 1g). Considering the energy dispersion feature, observation location (MLT =  $\sim 2.1$  hr), and the time interval ( $\sim 15$  min) between electron flux enhancement and the increase in the AE index, these enhancements of energetic electrons are caused by substorm injections. It is worth noting that as the energetic electron fluxes increase, the intensity of chorus waves is simultaneously amplified as shown in Figures 1b, 1c, 1f, and 1g. Before the enhancement of electron fluxes ( $\sim 12:30$ – $13:00$  UT), the wave electric spectral density is about  $10^{-5} (\text{mV/m})^2/\text{Hz}$ , and the wave magnetic spectral density is almost undetectable by the PWE instrument ( $\sim 10^{-2} \text{ pT}^2/\text{Hz}$ ); after the enhancement of electron fluxes ( $\sim 13:00$ – $13:30$  UT), the wave electric spectral density increases to  $\sim 10^{-2} (\text{mV/m})^2/\text{Hz}$ , and the wave magnetic spectral density is  $\sim 10 \text{ pT}^2/\text{Hz}$ . As a result, the wave power increases by about three orders of magnitude, suggesting the significant effect of these enhanced energetic electron fluxes on the evolution of chorus waves.

During the time interval, the Arase satellite also recorded some burst waveform data (with a high sampling rate of 65 kHz), and the spectra of two examples are presented in Figure 2: one is observed at  $\sim 12:36:45$  UT (before the enhancement of electron fluxes, T0), and the other is observed at  $\sim 13:01:30$  UT (after the enhancement of electron fluxes, T1). Figure 2a shows the wave spectrum of the electric field: before the enhancement of electron fluxes, the wave spectrum displays weak and fuzzy rising-tone structures in the frequency range from  $\sim 800$  to  $2500$  Hz; while after the enhancement of electron fluxes, the wave spectrum presents intense and discrete rising-





**Figure 3.** (a) Electron phase space density (PSD) in the energy range  $\sim 7$ –1,000 keV at time T0 where  $\sim 7$ –80 keV electrons are measured by MEPe and  $\sim 80$ –1,000 keV electrons are measured by high-energy electron experiments (HEP), (b) the pitch angles of electrons satisfying the first-order cyclotron resonance condition for parallel propagating chorus waves at three normalized frequencies, (c) the logarithm of PSD of resonant electrons with pitch angles equal to  $90^\circ$  as a function of energy, and (d) the defined  $f^*$  as a function of  $E \cos^2 \alpha / (m_e c^2 / 2)$ , where the data points from MEPe and HEP are marked by gray and yellow colors, respectively; (e–h) the results at time T1 in the same format as panels (a–d). In panels (c, d, g, and h), the lines are the fitting curves based on the least squares method, and the triangles are calculated based on the observation data.

tone elements in the frequency range from  $\sim 550$  to 1,900 Hz. These chorus waves at times T0 and T1 are quasi-parallel with small wave normal angles and propagate in an anti-parallel direction relative to the background magnetic field (Figures 2c, 2d, 2g, and 2h).

One-hour overview in Figure 1 shows the simultaneous observations of enhanced energetic electron fluxes and amplified chorus wave intensity, implying the potential relation between the chorus wave evolution and the enhanced electron fluxes. Furthermore, two 15-sec chorus wave examples in Figure 2 indicate that these weak and fuzzy chorus waves evolve into intense and discrete rising-tone elements as the fluxes of energetic electrons increase. These observational characteristics suggest that nonlinear processes play an important role during the evolution of chorus waves. To further verify the conjecture, both linear and nonlinear theoretical analyses are conducted on the two examples.

Figure 3a shows the electron phase space density (PSD) as a function of energy, where black symbols represent the PSD in the perpendicular direction, and red and blue symbols represent the PSD in the nearly parallel direction, respectively. Both electron PSDs at times T0 and T1 show a pitch angle anisotropy. The profile of the PSDs is quite similar for electrons with energy less than  $\sim 20$  keV, while for electrons in the energy range of  $\sim 20$ –200 keV, the PSD at time T1 is much larger than that at time T0, which is consistent with the electron spectrum shown in Figures 1f and 1g. Based on the electron count measured by MEPe and HEP, we estimated the coefficient of variation CV (Poisson noise) assuming that the measurement follows a Poisson distribution (Kurita et al., 2025). The equation is as follows:  $CV = \sqrt{C}/C = 1/\sqrt{C}$ , where  $C$  is the electron counts. The coefficient of variation is  $<10\%$  for MEPe electrons,  $\sim 15\%$ – $30\%$  for HEP electrons in the energy range of 82.5–109.5 keV, and  $\sim 50\%$ – $60\%$  for HEP electrons in the energy range of 416.5–503.5 keV. Based on the cold plasma dispersion relation, Figures 3b and 3f show the minimum cyclotron resonance energy as a function of pitch angle. Using the same method as Kubota et al. (2018), we first obtain the resonance energy ranges 50–470 keV and 37–420 keV for the events at T0 and T1, respectively, and then assume that the velocity distribution function of energetic electrons is represented by a bi-Maxwellian distribution:

$$f(E, \alpha) = f_0 \exp\left(-\frac{v_{\parallel}^2}{2v_{h\parallel,loc}^2} - \frac{v_{\perp}^2}{2v_{h\perp,loc}^2}\right) = f_0 \exp\left(-\frac{E \cos^2 \alpha}{m_e v_{h\parallel,loc}^2} - \frac{E \sin^2 \alpha}{m_e v_{h\perp,loc}^2}\right), \quad (1)$$

where  $m_e$  is the electron mass,  $E$  is the kinetic energy of electrons, and  $\alpha$  is the pitch angle. We assume that  $f_0$  and thermal velocities are constant values in the resonance energy range. Substituting  $\alpha = 90^\circ$  into Equation 1, we can obtain the equation:

$$\ln f(E, \alpha = 90^\circ) = \ln f_0 - \frac{E}{m_e v_{h\perp,loc}^2} \quad (2)$$

Using the observed electron PSD at  $\alpha = 90^\circ$  in the resonance energy range, the calculated values of  $\ln f(E, \alpha = 90^\circ)$  at times T0 and T1 are shown as triangles in Figures 3c and 3g, respectively. The perpendicular thermal velocity  $v_{h\perp,loc}$  can be calculated from the slope of the fitting curve (red lines show the fitting curves), and the values of  $v_{h\perp,loc}$  are 0.374c and 0.305c (c is the speed of light) for the events at times T0 and T1, respectively. Then using the perpendicular thermal velocity  $v_{h\perp,loc}$ , we construct a new function as follows:

$$f^*(E, \alpha, v_{h\perp,loc}) = \ln f(E, \alpha) + \frac{E \sin^2 \alpha}{m_e v_{h\perp,loc}^2}, \quad (3)$$

and then substituting Equation 1 into Equation 3, we can obtain:

$$f^*(E, \alpha, v_{h\perp,loc}) = \ln f_0 - \frac{v_{\parallel}^2}{2v_{h\parallel,loc}^2}. \quad (4)$$

Using the observed electron PSD in the resonance energy range and  $\alpha = 0-180^\circ$ , the values of  $f^*(E, \alpha, v_{h\perp,loc})$  could be obtained and their relationship with  $v_{\parallel}^2$  (where  $v_{\parallel}^2$  is equal to  $2E \cos^2 \alpha / m_e$ ) at times T0 and T1 are shown as triangles in Figures 3d and 3h, respectively. The parallel thermal velocity  $v_{h\parallel,loc}$  can be calculated from the slope of the fitting curve (blue lines show the fitting curves), and the values of  $v_{h\parallel,loc}$  are 0.352c and 0.285c for the events at times T0 and T1, respectively. In addition, the hot electron density  $n_{h,loc}$  can be estimated by integrating the electron PSD in the resonance energy range, and the values are  $0.0048 \text{ cm}^{-3}$  and  $0.034 \text{ cm}^{-3}$ , respectively.

Previous studies have indicated that chorus waves are usually generated by the anisotropic energetic electrons in the minimum-B region, such as the magnetic equator (e.g., W. Li, Thorne, Angelopoulos, Bortnik, et al., 2009; Ma et al., 2022; Tsurutani & Smith, 1977) and high-latitude minimum-B pockets (Tsurutani et al., 2009; Vaivads et al., 2007). Considering the wave propagation direction and location in this event, these chorus waves are likely generated at the magnetic equator. Therefore, the hot electron parameters estimated at the satellite location ( $n_{h,loc}$ ,  $v_{h\parallel,loc}$ , and  $v_{h\perp,loc}$ ) need to be transformed into equatorial values ( $n_{h,eq}$ ,  $v_{h\parallel,eq}$ , and  $v_{h\perp,eq}$ ), where the transformation method is based on Liouville's theorem that the distribution function is preserved along the field line with the conservation of the first adiabatic invariant and the particle total kinetic energy (the detailed equations can be found in Summers et al., 2012). The equations describing the relation between the equatorial and off-equatorial hot electron parameters are as follows:

$$\frac{n_{h,loc}}{v_{h\parallel,loc} v_{h\perp,loc}^2} = \frac{n_{h,eq}}{v_{h\parallel,eq} v_{h\perp,eq}^2} \quad (5)$$

$$v_{h\parallel,loc}^2 = v_{h\parallel,eq}^2 \quad (6)$$

$$\frac{1}{v_{h\perp,loc}^2} = \left(1 - \frac{B_{eq}}{B_{loc}}\right) \frac{1}{v_{h\perp,eq}^2} + \frac{B_{eq}}{B_{loc}} \cdot \frac{1}{v_{h\perp,eq}^2} \quad (7)$$

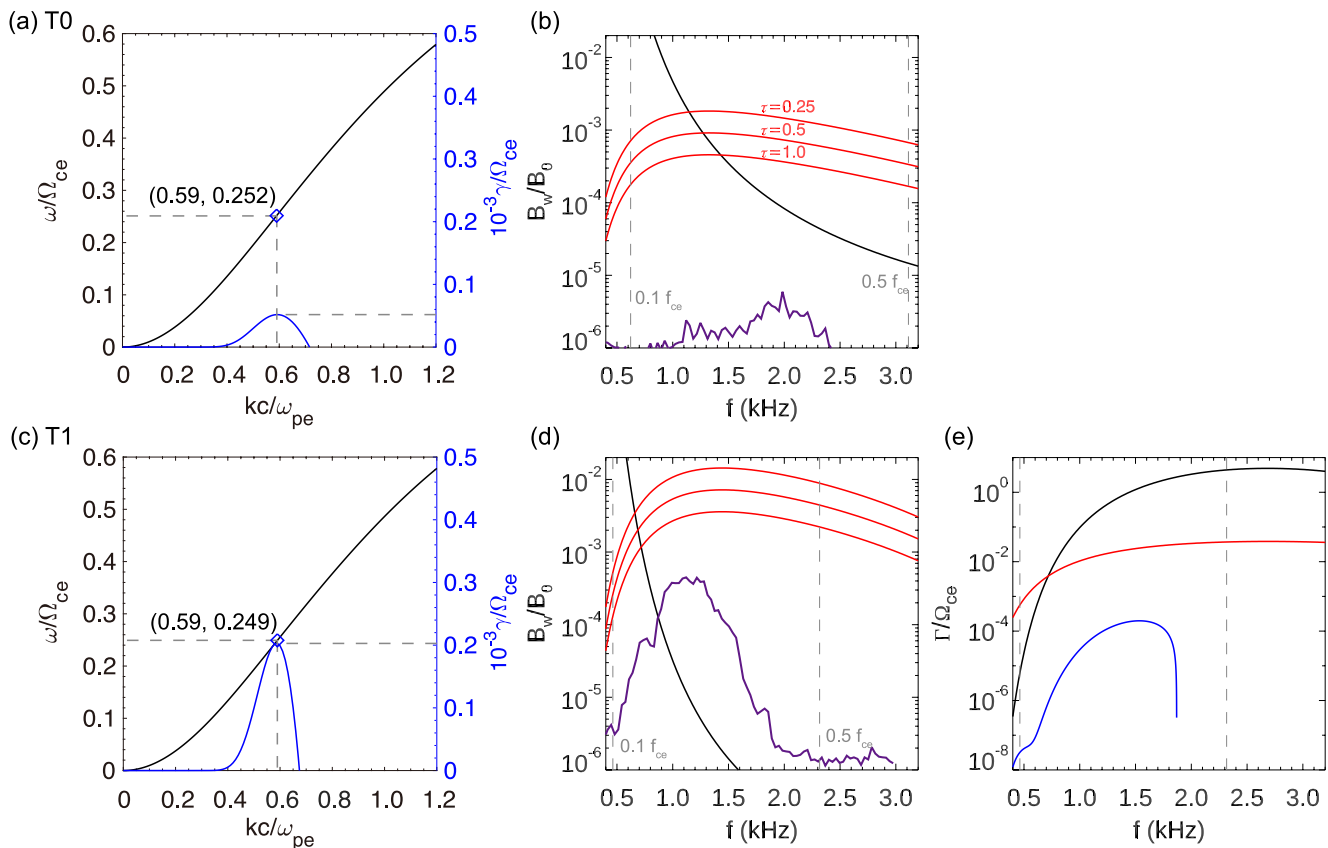
Both local and equatorial parameters are presented in Table 1. The hot electron density at time T1 is about 7 times that at time T0, which agrees with the observed electron spectrum.

**Table 1**  
The Local and Equatorial Electron Parameters and Background Magnetic Fields

Local	$n_{e,loc}/\text{cm}^{-3}$	$B_{loc}/\text{nT}$	$n_{h,loc}/\text{cm}^{-3}$	$v_{h\parallel,loc}$	$v_{h\perp,loc}$
T0	2.69	640.5	0.0048	0.352c	0.374c
T1	1.82	391.8	0.0340	0.285c	0.305c
Equatorial	$n_{e,eq}/\text{cm}^{-3}$	$B_{eq}/\text{nT}$	$n_{h,eq}/\text{cm}^{-3}$	$v_{h\parallel,eq}$	$v_{h\perp,eq}$
T0	2.69	222.3	0.0063	0.352c	0.430c
T1	1.82	165.5	0.0424	0.285c	0.341c

Using the BO dispersion solver (Xie, 2019), we calculate the dispersion relation and linear growth rate of whistler mode waves based on the equatorial electron parameters and background magnetic fields. Figures 4a and 4c show calculated dispersion relations and linear growth rates. At times T0 and T1, The peak values of linear growth rate are  $\sim 0.52 \times 10^{-4}/\Omega_{ce}$  and  $\sim 2.0 \times 10^{-4}/\Omega_{ce}$ , and the wave frequencies at which the linear growth rate reaches the peak value are  $\sim 0.252 f_{ce}$  and  $0.249 f_{ce}$ , respectively, which is consistent with the observations.

We further perform nonlinear theoretical analysis by calculating the threshold amplitude, optimum amplitude, and nonlinear growth rate (using Equations 105, 97, and 92 in Omura, 2021). The geomagnetic field configurations at times T0 and T1 calculated by GEOPACK-2008 are constructed by the International Geomagnetic Reference Field (IGRF-13) and TS05 magnetic field model (Tsyganenko & Sitnov, 2005). Assuming a parabolic geomagnetic field  $B = B_{eq}(1 + ah^2)$  near the magnetic equator (e.g., Katoh & Omura, 2007) where  $h$  is the distance from the magnetic equator along the dipole magnetic field line, we can obtain the inhomogeneity  $a$ , and



**Figure 4.** (a, c) Linear theoretical analysis results (black line represents the dispersion relation, and blue line represents the linear growth rate), (b, d) the threshold amplitude (black), optimum amplitude (red), and observational amplitude (purple), and (e) the nonlinear growth rates for threshold amplitude (black) and optimum amplitude (red) ( $\tau = 1.0$ ). The linear growth rate in panel c is also plotted as blue lines in panel (e).

the values are 0.448 and 0.433 at times T0 and T1, respectively. Similar values of inhomogeneity show that the geomagnetic field configuration remains almost unchanged after the enhancement of energetic electron fluxes. Based on previous studies (e.g., Kubota et al., 2018), the ratio of the nonlinear transition time to nonlinear trapping period  $\tau$  is adopted as 0.25, 0.5, and 1.0, and the depth of an electron hole is set as 0.5. Using these parameters and those listed in Table 1, we calculate the threshold amplitude  $B_{th}$  and optimum amplitude  $B_{op}$  at the magnetic equator, which are respectively presented in black lines and red lines in Figure 4b (4d) for the event at time T0 (T1). In addition, the observed wave amplitudes are also superposed in the figure by purple lines. For the event at time T0 (before the enhancement of energetic electron fluxes), the observed wave amplitude is smaller than the threshold amplitude, indicating that there is no nonlinear growth or the nonlinear growth is quite weak at time T0; for the event at time T1 (after the enhancement of energetic electron fluxes), the threshold amplitudes decrease significantly, and the observed wave amplitude exceeds the threshold amplitude in the wave frequency range above  $\sim 900$  Hz, indicating that the nonlinear growth plays a significant role in the evolution of chorus wave at frequencies greater than  $\sim 900$  Hz. Figure 4e shows the nonlinear growth rate calculated using optimum amplitudes ( $\tau = 1.0$ ) by red line and the nonlinear growth rate calculated using threshold amplitude by black line. The nonlinear growth rate ( $\sim 10^{-2}$ ) is much larger than the linear growth rate ( $\sim 10^{-4}$ , blue lines); thus, nonlinear growth plays an important role in the amplification and spectral evolution of chorus waves, explaining the significant difference between the chorus waves at times T0 and T1.

#### 4. Summary and Discussion

Using the Arase satellite data, we present direct evidence for the nonlinear evolution of chorus waves following a substorm injection, emphasizing the significant role of nonlinear processes in chorus wave amplification and spectral evolution. Prior to the substorm injection, the chorus wave spectrum appears as a weak and fuzzy rising-tone structure; the substorm injection causes the enhancement of energetic electron fluxes (i.e.,  $\sim 20$ – $200$  keV), and the chorus waves observed at the same time exhibit clear and intense rising-tone elements. Linear theoretical analysis showed that anisotropic energetic electrons provide free energy for the generation of seed chorus waves, and the enhancement of energetic electrons increases the linear growth rate. Nonlinear theoretical analysis showed that the increase in energetic electrons reduces the threshold amplitude, facilitating the entry of chorus waves into the nonlinear growth process. At time T0, chorus waves undergo linear growth process but no (or weak) nonlinear growth process; at time T1, chorus waves undergo both linear growth and intense nonlinear growth processes, but the nonlinear growth rate is  $\sim 100$  times larger than the linear growth rate. Therefore, these analysis results indicate that nonlinear growth plays a more dominant role than linear effects in the amplification and spectral evolution of chorus waves.

Substorm injections usually lead to a significant enhancement of energetic electrons with anisotropy in the inner magnetosphere. In this study, the enhancement of  $\sim 20$ – $200$  keV electrons due to a substorm injection was observed by the Arase satellite, and the resonant electron density at time T1 is about seven times that at time T0; the anisotropy at time T1 is slightly larger than that at time T0. Since the linear growth rate depends on the fraction of electrons resonating with the waves and the electron anisotropy, the linear growth rate at time T1 is larger (Figures 4a and 4d). Although the increase in linear growth rate is consistent with the increase in chorus wave intensity, observations showed that there are clear differences in the spectra of the chorus waves at T0 and T1 (Figure 2), which cannot be explained by linear theory. Furthermore, the nonlinear theoretical analysis demonstrated that the threshold amplitude at time T1 is much smaller than that at time T0; therefore, the chorus waves at time T1 can easily satisfy the nonlinear growth condition, whereas the chorus waves at time T0 do not satisfy the nonlinear growth condition. As a result, the enhancement of energetic electrons caused by the substorm injection reduces the threshold amplitude of nonlinear growth, which is the key factor driving the nonlinear evolution of chorus waves, even if the linear growth rate is not sufficient.

Linear theoretical calculations in Figures 4a and 4c show that the maximum linear growth rate peaks at a similar frequency  $\sim 0.25 f_{ce}$  at both T0 and T1, which is slightly different from the observations, that is, T0:  $\sim 2000$  Hz ( $0.32 f_{ce}$ ); T1:  $\sim 1,000$  Hz ( $0.22 f_{ce}$ ). This discrepancy between observations and linear theoretical calculations may be related to several factors. First, nonlinear growth plays a significant role in the amplification and spectral evolution of chorus waves, as its growth rate is significantly larger than that of linear growth. Second, we estimated the hot electron parameters by approximating the distribution of hot electrons with a bi-Maxwellian distribution function, which is generally consistent with the observation data but not exactly the same.



Furthermore, due to the limitations of in situ observation, the hot electron distribution was measured after the wave generation, which may not fully reflect the electron distribution before the wave excitation. Therefore, these factors may collectively contribute to the discrepancy between observations and linear theoretical calculations.

## Data Availability Statement

Science data of the ERG (Arase) satellite were obtained from the ERG Science Center operated by ISAS/JAXA and ISEE/Nagoya University (Miyoshi, Hori et al., 2018). In this study, we used PWE/OFA-L2 power spectrum data v02\_03 (Y. Kasahara et al., 2018), PWE/WFC-L2 electric field waveform data v01\_01 (Y. Kasahara et al., 2020a) and magnetic field waveform data v01\_01 (Y. Kasahara et al., 2020b), PWE/HFA-L3 electron density data v04\_08 (Y. Kasahara et al., 2021), MEPE-L2 omniflux v01\_01 (S. Kasahara et al., 2018b) and -L3 pitch angle sorted flux data v01\_01 (S. Kasahara et al., 2022), HEP-L3 pitch angle sorted flux data v01\_01 (Hori et al., 2020), MGF-L2 8 s spin-averaged data v03\_04 (Matsuoka et al., 2018), and Orbit-L2 v03 data (Miyoshi, Shinohara, & Jun, 2018). The AE index can be obtained from OMNIWeb (<https://omniweb.gsfc.nasa.gov/>; Nose et al., 2015). The data analysis was carried out using the Space Physics Environment Data Analysis System (SPEDAS; Angelopoulos et al., 2019) and the “ERG-SC” plug-in tools (Miyoshi, Hori et al., 2018). The GEOPACK-2008 package is available at <https://geo.phys.spbu.ru/~tsyganenko/empirical-models/>.

## Acknowledgments

This research is supported by JSPS grants (22K21345, 22KK0046, 23K25925, 24H00751, 21H04526). We also acknowledge the entire ERG science team for the use of their data.

## References

- Agapitov, O. V., Artemyev, A. V., Mourenas, D., Mozer, F. S., & Krasnoselskikh, V. (2015). Empirical model of lower band chorus wave distribution in the outer radiation belt. *Journal of Geophysical Research: Space Physics*, 120(12), 10425–10442. <https://doi.org/10.1002/2015JA021829>
- Allison, H. J., & Shprits, Y. Y. (2020). Local heating of radiation belt electrons to ultra-relativistic energies. *Nature Communications*, 11(1), 4533. <https://doi.org/10.1038/s41467-020-18053-z>
- Angelopoulos, V., Cruce, P., Drozdov, A., Grimes, E. W., Hatzigeorgiou, N., King, D. A., et al. (2019). The Space Physics Environment Data Analysis System (SPEDAS). *Space Science Reviews*, 215(1). <https://doi.org/10.1007/s11214-018-0576-4>
- Bortnik, J., & Thorne, R. M. (2007). The dual role of ELF/VLF chorus waves in the acceleration and precipitation of radiation belt electrons. *Journal of Atmospheric and Solar-Terrestrial Physics*, 69(3), 378–386. <https://doi.org/10.1016/j.jastp.2006.05.030>
- Burtis, W. J., & Helliwell, R. A. (1969). Banded chorus-A new type of VLF radiation observed in the magnetosphere by OGO 1 and OGO 3. *Journal of Geophysical Research*, 74(11), 3002–3010. <https://doi.org/10.1029/ja074i011p03002>
- Chen, H., Lu, Q., Wang, X., Fan, K., Chen, R., & Gao, X. (2022a). One-dimensional gcPIC-6f simulation of hooked chorus waves in the Earth's inner magnetosphere. *Geophysical Research Letters*, 49(4), e2022GL097989. <https://doi.org/10.1029/2022GL097989>
- Chen, H., Wang, X., Chen, L., Omura, Y., Tsurutani, B. T., Lin, Y., & Xia, Z. (2023a). Evolution of chorus subpackets in the Earth's magnetosphere. *Geophysical Research Letters*, 50(21), e2023GL105938. <https://doi.org/10.1029/2023GL105938>
- Chen, H., Wang, X., Chen, L., Zhang, X.-J., Omura, Y., Chen, R., et al. (2024a). Nonlinear electron trapping through cyclotron resonance in the formation of chorus subpackets. *Geophysical Research Letters*, 51(11), e2024GL109481. <https://doi.org/10.1029/2024GL109481>
- Chen, R., Gao, X., Lu, Q., Tsurutani, B. T., Miyoshi, Y., Zhou, X., et al. (2023b). Observation of whistler mode waves inside mirror mode structures in the Earth's outer magnetosphere. *Journal of Geophysical Research: Space Physics*, 128(11), e2023JA031792. <https://doi.org/10.1029/2023JA031792>
- Chen, R., Miyoshi, Y., Gao, X., Lu, Q., Tsurutani, B. T., Hosokawa, K., et al. (2024b). Observational evidence for three time-scale modulations in the pulsating aurora. *Geophysical Research Letters*, 51(16), e2024GL108253. <https://doi.org/10.1029/2024GL108253>
- Chen, R., Tsurutani, B. T., Gao, X., Lu, Q., Chen, H., Lakhina, G. S., & Hajra, R. (2022b). The structure and microstructure of rising-tone chorus with frequencies crossing at  $f \sim 0.5f_{ce}$ . *Journal of Geophysical Research: Space Physics*, 127(8), e2022JA030438. <https://doi.org/10.1029/2022JA030438>
- Gao, X., Chen, R., Lu, Q., Chen, L., Chen, H., & Wang, X. (2022). Observational evidence for the origin of repetitive chorus emissions. *Geophysical Research Letters*, 49(12), e2022GL099000. <https://doi.org/10.1029/2022GL099000>
- Gao, X., Li, W., Thorne, R. M., Bortnik, J., Angelopoulos, V., Lu, Q., et al. (2014). New evidence for generation mechanisms of discrete and hiss-like whistler mode waves. *Geophysical Research Letters*, 41(14), 4805–4811. <https://doi.org/10.1002/2014GL060707>
- Gao, X., Ma, J., Shao, T., Chen, R., Ke, Y., & Lu, Q. (2023). Why chorus waves are the dominant driver for diffuse auroral precipitation. *Science Bulletin*, 69(5), 597–600. <https://doi.org/10.1016/j.scib.2023.12.009>
- Hori, T., Mitani, T., Matsuoka, A., Teramoto, M., Park, I., Takashima, T., et al. (2020). The HEP instrument Level-3 pitch angle sorted electron flux data of exploration of energization and radiation in geospace (ERG) arase satellite [Dataset]. *ERG*. <https://doi.org/10.34515/DATA.ERG-01002>
- Horne, R. B., Thorne, R. M., Glauert, S. A., Albert, J. M., Meredith, N. P., & Anderson, R. R. (2005). Timescale for radiation belt electron acceleration by whistler mode chorus waves. *Journal of Geophysical Research*, 110(A3), A03225. <https://doi.org/10.1029/2004JA010811>
- Kasahara, S., Miyoshi, Y., Yokota, S., Mitani, T., Kasahara, Y., Matsuda, S., et al. (2018). Pulsating aurora from electron scattering by chorus waves. *Nature*, 554(7692), 337–340. <https://doi.org/10.1038/nature25505>
- Kasahara, S., Yokota, S., Hori, T., Keika, K., Miyoshi, Y., & Shinohara, I. (2018). The MEP-e instrument level-2 omni-directional flux data of exploration of energization and radiation in geospace (ERG) arase satellite [Dataset]. *ERG*. <https://doi.org/10.34515/DATA.ERG-02001>
- Kasahara, S., Yokota, S., Matsuoka, A., Hori, T., Keika, K., Teramoto, M., et al. (2022). The MEP-e instrument level-3 pitch-angle sorted flux data of Exploration of energization and radiation in geospace (ERG) arase satellite [Dataset]. *ERG*. <https://doi.org/10.34515/DATA.ERG-02003>
- Kasahara, Y., Kojima, H., Matsuda, S., Ozaki, M., Yagitani, S., Shoji, M., et al. (2018). The PWE/OFA instrument Level-2 power spectrum data of exploration of energization and radiation in geospace (ERG) arase satellite [Dataset]. *ERG*. <https://doi.org/10.34515/DATA.ERG-08000>

- Kasahara, Y., Kojima, H., Matsuda, S., Shoji, M., Nakamura, S., Kitahara, M., et al. (2020a). The PWE/WFC instrument Level-2 electric field waveform data of exploration of energization and radiation in geospace (ERG) arase satellite [Dataset]. *ERG*. <https://doi.org/10.34515/DATA.ERG-09000>
- Kasahara, Y., Kojima, H., Matsuda, S., Shoji, M., Nakamura, S., Kitahara, M., et al. (2020b). The PWE/WFC instrument Level-2 electric field spectrum data of exploration of energization and radiation in geospace (ERG) arase satellite [Dataset]. *ERG*. <https://doi.org/10.34515/DATA.ERG-09002>
- Kasahara, Y., Kumamoto, A., Tsuchiya, F., Kojima, H., Matsuda, S., Matsuoka, A., et al. (2021). The PWE/HFA instrument level-3 electron density data of exploration of energization and radiation in geospace (ERG) arase satellite [Dataset]. *ERG*. <https://doi.org/10.34515/DATA.ERG-10001>
- Kato, Y., & Omura, Y. (2007). Computer simulation of chorus wave generation in the Earth's inner magnetosphere. *Geophysical Research Letters*, 34(3), L03102. <https://doi.org/10.1029/2006GL028594>
- Kazama, Y., Miyoshi, Y., Kojima, H., Kasahara, Y., Kasahara, S., Usui, H., et al. (2021). Arase observation of simultaneous electron scatterings by upper-band and lower-band chorus emissions. *Geophysical Research Letters*, 48(14), e2021GL093708. <https://doi.org/10.1029/2021GL093708>
- Ke, Y., Gao, X., Lu, Q., Wang, X., & Wang, S. (2017). Generation of rising-tone chorus in a two-dimensional mirror field by using the general curvilinear PIC code. *Journal of Geophysical Research: Space Physics*, 122(8), 8154–8165. <https://doi.org/10.1002/2017JA024178>
- Kennel, C. F., & Petschek, H. E. (1966). Limit on stably trapped particle fluxes. *Journal of Geophysical Research*, 71(1), 1–28. <https://doi.org/10.1029/JZ071i001p00001>
- Kubota, Y., Omura, Y., Kletzing, C., & Reeves, G. (2018). Generation process of large-amplitude upper-band chorus emissions observed by van allen probes. *Journal of Geophysical Research: Space Physics*, 123(5), 3704–3713. <https://doi.org/10.1029/2017ja024782>
- Kumamoto, A., Tsuchiya, F., Kasahara, Y., Kasaba, Y., Kojima, H., Yagitani, S., et al. (2018). High frequency analyzer (HFA) of plasma wave experiment (PWE) onboard the Arase spacecraft. *Earth Planets and Space*, 70(1), 82. <https://doi.org/10.1186/s40623-018-0854-0>
- Kurita, S., Miyoshi, Y., Saito, S., Kasahara, S., Kato, Y., Matsuda, S., et al. (2025). Detection of ultrafast electron energization by whistler-mode chorus waves in the magnetosphere of Earth. *Scientific Reports*, 15(1), 992. <https://doi.org/10.1038/s41598-024-80693-8>
- Li, L., Omura, Y., Zhou, X.-Z., Zong, Q.-G., Rankin, R., Yue, C., & Fu, S.-Y. (2022). Nonlinear wave growth analysis of chorus emissions modulated by ULF waves. *Geophysical Research Letters*, 49(10), e2022GL097978. <https://doi.org/10.1029/2022GL097978>
- Li, W., Bortnik, J., Nishimura, Y., Thorne, R. M., & Angelopoulos, V. (2012). The origin of pulsating aurora: Modulated whistler mode chorus. In A. Keiling, E. Donovan, F. Bagenal, & T. Karlsson (Eds.), *Auroral phenomenology and magnetospheric processes: Earth and other planets* (Vol. 197, pp. 379–388). AGU. <https://doi.org/10.1029/2011GM001164>
- Li, W., Bortnik, J., Thorne, R. M., & Angelopoulos, V. (2011). Global distribution of wave amplitudes and wave normal angles of chorus waves using THEMIS wave observations: Chorus wave distribution on THEMIS. *Journal of Geophysical Research*, 116(A12), A12205. <https://doi.org/10.1029/2011JA017035>
- Li, W., Thorne, R. M., Angelopoulos, V., Bonnell, J. W., McFadden, J. P., Carlson, C. W., et al. (2009). Evaluation of whistler-mode chorus intensification on the night side during an injection event observed on the THEMIS spacecraft. *Journal of Geophysical Research*, 114(A1), A00C14. <https://doi.org/10.1029/2008JA013554>
- Li, W., Thorne, R. M., Angelopoulos, V., Bortnik, J., Cully, C. M., Ni, B., et al. (2009). Global distribution of whistler-mode chorus waves observed on the THEMIS spacecraft. *Geophysical Research Letters*, 36(9), L09104. <https://doi.org/10.1029/2009GL037595>
- Li, W., Thorne, R. M., Bortnik, J., Nishimura, Y., Angelopoulos, V., Chen, L., et al. (2010). Global distributions of suprathermal electrons observed on THEMIS and potential mechanisms for access into the plasmasphere. *Journal of Geophysical Research*, 115(A12), A00J10. <https://doi.org/10.1029/2010JA015687>
- Li, W., Thorne, R. M., Ma, Q., Ni, B., Bortnik, J., Baker, D. N., et al. (2014). Radiation belt electron acceleration by chorus waves during the 17 March 2013 storm. *Journal of Geophysical Research: Space Physics*, 119(6), 4681–4693. <https://doi.org/10.1002/2014JA019945>
- Lu, Q., Chen, L., Wang, X., Gao, X., Lin, Y., & Wang, S. (2021). Repetitive emissions of rising-tone chorus waves in the inner magnetosphere. *Geophysical Research Letters*, 48(15), e2021GL094979. <https://doi.org/10.1029/2021GL094979>
- Lu, Q., Ke, Y., Wang, X., Liu, K., Gao, X., Chen, L., & Wang, S. (2019). Two-dimensional general curvilinear particle-in-cell (gcPIC) simulation of rising-tone chorus waves in a dipole magnetic field. *Journal of Geophysical Research: Space Physics*, 124(6), 4157–4167. <https://doi.org/10.1029/2019JA026586>
- Ma, J., Gao, X., Chen, H., Tsurutani, B. T., Ke, Y., Chen, R., & Lu, Q. (2022). The effects of substorm injection of energetic electrons and enhanced solar wind ram pressure on whistler-mode chorus waves: A statistical study. *Journal of Geophysical Research: Space Physics*, 127(11), e2022JA030502. <https://doi.org/10.1029/2022JA030502>
- Matsuda, S., Kasahara, Y., Kojima, H., Kasaba, Y., Yagitani, S., Ozaki, M., et al. (2018). Onboard software of plasma wave experiment aboard Arase: Instrument management and signal processing of waveform capture/onboard frequency analyzer. *Earth Planets and Space*, 70(1), 75. <https://doi.org/10.1186/s40623-018-0838-0>
- Matsuoka, A., Teramoto, M., Imajo, S., Kurita, S., Miyoshi, Y., & Shinohara, I. (2018). The MGF instrument Level-2 spin-averaged magnetic field data of Exploration of energization and radiation in geospace (ERG) Arase satellite [Dataset]. *ERG*. <https://doi.org/10.34515/DATA.ERG-06001>
- Meredith, N. P., Horne, R. B., Thorne, R. M., & Anderson, R. R. (2003). Favored regions for chorus-driven electron acceleration to relativistic energies in the Earth's outer radiation belt. *Geophysical Research Letters*, 30(16), 1871. <https://doi.org/10.1029/2003GL017698>
- Mitani, T., Takashima, T., Kasahara, S., Miyake, W., & Hirahara, M. (2018). High-energy electron experiments (HEP) aboard the ERG (Arase) satellite. *Earth Planets and Space*, 70(1), 77. <https://doi.org/10.1186/s40623-018-0853-1>
- Miyoshi, Y., Hori, T., Shoji, M., Teramoto, M., Chang, T. F., Matsuda, S., et al. (2018). The ERG science center. *Earth Planets and Space*, 70(1), 96. <https://doi.org/10.1186/s40623-018-0867-8>
- Miyoshi, Y., Hosokawa, K., Kurita, S., Oyama, S.-I., Ogawa, Y., Saito, S., et al. (2021). Penetration of MeV electrons into the mesosphere accompanying pulsating aurorae. *Scientific Reports*, 11(1). <https://doi.org/10.1038/s41598-021-92611-3>
- Miyoshi, Y., Kataoka, R., Kasahara, Y., Kumamoto, A., Nagai, T., & Thomsen, M. F. (2013). High-speed solar wind with southward interplanetary magnetic field causes relativistic electron flux enhancement of the outer radiation belt via enhanced condition of whistler waves. *Geophysical Research Letters*, 40(17), 4520–4525. <https://doi.org/10.1002/grl.50916>
- Miyoshi, Y., Kato, Y., Nishiyama, T., Sakanoi, T., Asamura, K., & Hirahara, M. (2010). Time of flight analysis of pulsating aurora electrons, considering wave-particle interactions with propagating whistler mode waves. *Journal of Geophysical Research*, 115(A10), A10312. <https://doi.org/10.1029/2009JA015127>
- Miyoshi, Y., Morioka, A., Kataoka, R., Kasahara, Y., & Mukai, T. (2007). Evolution of the outer radiation belt during the November 1993 storms driven by corotating interaction regions. *Journal of Geophysical Research*, 112(A5), A05210. <https://doi.org/10.1029/2006JA012148>

- Miyoshi, Y., Morioka, A., Misawa, H., Obara, T., Nagai, T., & Kasahara, Y. (2003). Rebuilding process of the outer radiation belt during the 3 November 1993 magnetic storm: NOAA and Exos-D observations. *Journal of Geophysical Research*, 108(A1), 1004. <https://doi.org/10.1029/2001JA007542>
- Miyoshi, Y., Saito, S., Kurita, S., Asamura, K., Hosokawa, K., Sakanoe, T., et al. (2020). Relativistic electron microbursts as high-energy tail of pulsating aurora electrons. *Geophysical Research Letters*, 47(21), e2020GL090360. <https://doi.org/10.1029/2020GL090360>
- Miyoshi, Y., Shinohara, I., & Jun, C.-W. (2018). The level-2 orbit data of exploration of energization and radiation in geospace (ERG) Arase satellite [Dataset]. *EGR*. <https://doi.org/10.34515/DATA.ERG-12000>
- Miyoshi, Y., Shinohara, I., Takashima, T., Asamura, K., Higashio, N., Mitani, T., et al. (2018). Geospace exploration project ERG. *Earth Planets and Space*, 70(1), 101. <https://doi.org/10.1186/s40623-018-0862-0>
- Ni, B., Thorne, R. M., Shprits, Y. Y., & Bortnik, J. (2008). Resonant scattering of plasma sheet electrons by whistler-mode chorus: Contribution to diffuse auroral precipitation. *Geophysical Research Letters*, 35(11), L11106. <https://doi.org/10.1029/2008GL034032>
- Nogi, T., & Omura, Y. (2023). Upstream shift of generation region of whistler-mode rising-tone emissions in the magnetosphere. *Journal of Geophysical Research: Space Physics*, 128(3), e2022JA031024. <https://doi.org/10.1029/2022JA031024>
- Nose, M., Iyemori, T., Sugiura, M., & Kamei, T. (2015). Geomagnetic AE index [Dataset]. *World Data Center for Geomagnetism, Kyoto*. <https://doi.org/10.17593/15031-54800>
- Omura, Y. (2021). Nonlinear wave growth theory of whistler-mode chorus and hiss emissions in the magnetosphere. *Earth Planets and Space*, 73(1), 95. <https://doi.org/10.1186/s40623-021-01380-w>
- Reeves, G. D., Spence, H. E., Henderson, M. G., Morley, S. K., Friedel, R. H. W., Funsten, H. O., et al. (2013). Electron acceleration in the heart of the van allen radiation belts. *Science*, 341(6149), 991–994. <https://doi.org/10.1126/science.1237743>
- Santolík, O., Kletzing, C. A., Kurth, W. S., Hospodarsky, G. B., & Bounds, S. R. (2014). Fine structure of large-amplitude chorus wave packets. *Geophysical Research Letters*, 41(2), 293–299. <https://doi.org/10.1002/2013GL058889>
- Summers, D., Omura, Y., Miyashita, Y., & Lee, D.-H. (2012). Nonlinear spatiotemporal evolution of whistler mode chorus waves in Earth's inner magnetosphere. *Journal of Geophysical Research*, 117(A9), A09206. <https://doi.org/10.1029/2012ja017842>
- Thorne, R. M., Li, W., Ni, B., Ma, Q., Bortnik, J., Chen, L., et al. (2013). Rapid local acceleration of relativistic radiation-belt electrons by magnetospheric chorus. *Nature*, 504(7480), 411–414. <https://doi.org/10.1038/nature12889>
- Thorne, R. M., Ni, B., Tao, X., Horne, R. B., & Meredith, N. P. (2010). Scattering by chorus waves as the dominant cause of diffuse auroral precipitation. *Nature*, 467(7318), 943–946. <https://doi.org/10.1038/nature09467>
- Tsurutani, B. T., & Smith, E. J. (1974). Postmidnight chorus: A substorm phenomenon. *Journal of Geophysical Research*, 79(1), 118–127. <https://doi.org/10.1029/ja079i001p00118>
- Tsurutani, B. T., & Smith, E. J. (1977). Two types of magnetospheric ELF chorus and their substorm dependences. *Journal of Geophysical Research*, 82(32), 5112–5128. <https://doi.org/10.1029/JA082i032p05112>
- Tsurutani, B. T., Chen, R., Gao, X. L., Lu, Q. M., Pickett, J. S., Lakhina, G. S., et al. (2020). Lower-band “monochromatic” chorus riser subelement/wave packet observations. *Journal of Geophysical Research: Space Physics*, 125(10), e2020JA028090. <https://doi.org/10.1029/2020JA028090>
- Tsurutani, B. T., Lakhina, G. S., & Verkhoglyadova, O. P. (2013). Energetic electron (>10 keV) microburst precipitation, similar to 5–15s X-ray pulsations, chorus, and wave-particle interactions: A review. *Journal of Geophysical Research: Space Physics*, 118(5), 2296–2312. <https://doi.org/10.1002/jgra.50264>
- Tsurutani, B. T., Verkhoglyadova, O. P., Lakhina, G. S., & Yagitani, S. (2009). Properties of dayside outer zone chorus during HILDCAA events: Loss of energetic electrons. *Journal of Geophysical Research*, 114(A3), A03207. <https://doi.org/10.1029/2008JA013353>
- Tsyganenko, N., & Sitnov, M. (2005). Modeling the dynamics of the inner magnetosphere during strong geomagnetic storms. *Journal of Geophysical Research*, 110(A3), A03208. <https://doi.org/10.1029/2004JA010798>
- Vaivads, A., Santolík, O., Stenberg, G., André, M., Owen, C., Canu, P., & Dunlop, M. (2007). Source of whistler emissions at the dayside magnetopause. *Geophysical Research Letters*, 34(9), L09106. <https://doi.org/10.1029/2006GL029195>
- Wang, D., Shprits, Y. Y., Zhelavskaya, I. S., Agapitov, O. V., Drozdov, A. Y., & Aseev, N. A. (2019). Analytical chorus wave model derived from Van Allen Probe observations. *Journal of Geophysical Research: Space Physics*, 124(2), 1063–1084. <https://doi.org/10.1029/2018JA026183>
- Xiao, F. L., Su, Z. P., Zheng, H. N., & Wang, S. (2009). Modeling of outer radiation belt electron by multidimensional diffusion process. *Journal of Geophysical Research*, 114(A3), A03201. <https://doi.org/10.1029/2008JA013580>
- Xie, H. (2019). BO: A unified tool for plasma waves and instabilities analysis. *Computer Physics Communications*, 244, 343–371. <https://doi.org/10.1016/j.cpc.2019.06.014>
- Zhao, H., Baker, D. N., Li, X., Jaynes, A. N., & Kanekal, S. G. (2018). The acceleration of ultrarelativistic electrons during a small to moderate storm of 21 April 2017. *Geophysical Research Letters*, 45(12), 5818–5825. <https://doi.org/10.1029/2018GL078582>
- Zhao, H., Baker, D. N., Li, X., Malaspina, D. M., Jaynes, A. N., & Kanekal, S. G. (2019). On the acceleration mechanism of ultrarelativistic electrons in the center of the outer radiation belt: A statistical study. *Journal of Geophysical Research: Space Physics*, 124(11), 8590–8599. <https://doi.org/10.1029/2019JA027111>
- Zhou, X., Gao, X., Chen, R., Lu, Q., Ke, Y., Ma, J., & Kong, Z. (2023). Direct observation of rising-tone chorus triggered by enhanced solar wind pressure. *Journal of Geophysical Research: Space Physics*, 128(11), e2023JA031787. <https://doi.org/10.1029/2023JA031787>